To appear in:

Majlesi Journal of Electrical Engineering (MJEE)

Online ISSN: 2345-377X **Print ISSN:** 2345-3796

Received: 30-Apr-2025

Revised: 29-May-2025

Accepted: 18-Jul-2025

DOI: 10.57647/j.mjee.2025.17385

Original Research

Integrated Sensing and Communication-Assisted Orthogonal Time Frequency Space in a Non-Guard Band-Orthogonal Multiple Access Downlink Architecture for Vehicle-to-Infrastructure Networks

Ghasem Saeidi[1], Hamid Saeedi-Sourck[2]

1- Department of Electrical Engineering, Yazd University, Yazd, Iran.

Email: gh.saeidi@stu.yazd.ac.ir

2- Department of Electrical Engineering, Yazd University, Yazd, Iran.

Email: saeedi@yazd.ac.ir (Corresponding author) 0000-0002-8363-5030

Abstract

Orthogonal time frequency space (OTFS) modulation has emerged as a robust solution for high-mobility wireless communication and radar sensing by leveraging the delay-Doppler (DD) domain. This paper tackles challenges in resource allocation and multi-user interference (MUI) suppression in integrated sensing and communication (ISAC)-enabled vehicle-to-infrastructure (V2I) networks. We leverage a non-guard band-orthogonal multiple access (non-GB-OMA) scheme using interleaved DD-domain resource allocation with zero padding (ZP), thereby eliminating guard bands and reducing MUI. A two-dimensional (2D) correlation-based radar sensing method with an adaptive threshold detects user terminals (UTs), enabling UT-aware downlink resource allocation, channel estimation, and data detection. Channel estimation is treated as a sparse signal recovery problem, solved via the subspace pursuit (SP) algorithm using structured pilot patterns, a dedicated frame structure, and a specific external phase matrix. Furthermore, to combat high peak-to-average power ratio (PAPR) in OTFS systems, we employ low-power Zadoff-chu (Zch) and quadrature amplitude modulation (QAM) pilot sequences that maintain orthogonality and accuracy. Eventually, a two-stage feedback mechanism adapts the block linear-minimum mean square error (BL-MMSE) detector for data recovery. The proposed framework effectively manages PAPR, inter-symbol

interference (ISI), and MUI, enhancing V2I communication reliability and efficiency under high mobility. Simulation results demonstrate improved SNR and BER performance.

Keywords: Orthogonal time frequency space, Integrated sensing and communication, Orthogonal multiple access, Channel estimation, Data detection.

1. Introduction

The advent of 6G promises ultra-fast, reliable connectivity across diverse environments, supporting intelligent vehicular systems like V2X/V2I with advanced resource management [1], and expanding non-terrestrial networks to remote areas [2]. These developments reflect 6G's vision: seamless communication across terrestrial and space-based infrastructures [3].V2I is transforming the automotive industry by enabling vehicles to interact with infrastructure components such as roadside units (RSUs), traffic lights, and smart city systems. Stable communication and accurate sensing are essential for reliable vehicular networks [4]. Integrated sensing and communication (ISAC) technology addresses this need by enabling simultaneous communication and sensing, thereby enhancing functionality while reducing hardware costs and improving economic viability [5].

Several signal modulation techniques, such as orthogonal frequency division multiplexing (OFDM), have been employed in ISAC systems [6]. However, its performance degrades significantly in high-mobility environments, where doubly dispersive (time- and frequency-selective) channels pose severe challenges. These channels—characterized by rapid time variations and multipath propagation—induce inter-carrier interference (ICI) and inter-symbol interference (ISI), compromising signal integrity [7], [8], [9]. Although orthogonal frequency division multiplexing (OFDM) effectively combats static multipath propagation by employing cyclic prefixes, it is still vulnerable to Doppler shifts, which pose a significant challenge. The spectral broadening caused by Doppler effects undermines the orthogonality between subcarriers, leading to a decline in communication reliability [10]-[11] and radar sensing accuracy [12].

Recently, researchers have introduced a novel modulation technique known as orthogonal time frequency space (OTFS) [13], [14]. This approach is better suited for doubly selective channels by embedding data symbols in the delay-Doppler (DD) domain [14]-[16]. OTFS can be implemented using the Zak transform, which simplifies both transmitter and receiver design [13], [17]-[18]. Channel estimation in OTFS is further facilitated by the inherent sparsity of the DD domain [13], [14]. As a result, OTFS offers improved performance in high-mobility environments characterized by significant Doppler shifts and channel instability. For example,

[19] proposes a wavelet-based OTFS scheme for low Earth orbit (LEO) satellite systems to enhance robustness in time-varying channels, while [20] demonstrates its effectiveness in mitigating Doppler spread and ISI in 5G railway communications. However, it is important to emphasize that accurate channel state information (CSI) is not only essential but a prerequisite for the effective operation of OTFS systems [13], [21]-[23].

Despite significant research focused on enhancing OTFS communication performance in high-mobility scenarios [13]-[23], OTFS radar sensing remains relatively underexplored [24]-[31]. For instance, in [24] an OTFS-based ISAC system that leverages the maximum likelihood (ML) algorithm to precisely estimate target range and velocity, achieving superior communication performance over OFDM while hitting radar estimation performance bounds. In [25], an OTFS radar system utilizing a matched-filter algorithm is presented, effectively estimating targets, ranges, and velocities by distributing uniformly powered data symbols across the OTFS frame. Differently, [26] proposes a generalized likelihood ratio test-based detector using the OTFS, performing sensing directly in the time-domain (TD) and outperforming traditional FFT-based OFDM radar in estimation accuracy. Nonetheless, the untapped potential of OTFS sensing calls for deeper exploration. Notably, achieving high performance with the algorithm in [24] entails a computational complexity that scales cubically with frame size, presenting a considerable challenge. The successive interference cancellation (SIC) in the DD domain is applied in [27], though limited to single-user uplink scenarios. The exploration of 2D correlation-based parameter estimators is well-investigated in [28]-[31]. In [28], the design of ISAC using OTFS waveforms introduces a 2D correlation-based parameter estimator, conceptualized as a specialized pulse compression technique to enhance range-Doppler acquisition. A comprehensive ISAC framework employing OTFS modulation, where the 2D correlation method with parameter estimation is utilized for sensing purpose, is detailed in [29]. Additionally, a hybrid message passing (MP) detection algorithm has been organized to facilitate OTFS demodulation. A deep learning (DL)-based approach for target classification using OTFS signaling is introduced in [30]. This method enhances network performance by employing a 2D correlation technique for feature extraction during data preprocessing. Additionally, a deep neural network (DNN)-based scheme for radar target detection using OTFS was proposed by the authors in [31]. Prior to these works, a general deep learning-based multi-user (MU) radar detection framework was presented in [32], where a convolutional neural network (CNN) is trained to estimate target range and velocity directly from the range-Doppler map (RDM) of received radar signals. Although not specific to OTFS, this method is

highly applicable to OTFS-based ISAC systems due to its use of DD signal representations, as well as its strong robustness to noise and high prediction efficiency. However, the computational challenges and practical implementation aspects of DNN-based methods still require further investigation. While the aforementioned works focus on OTFS-specific ISAC designs, general waveform optimization strategies for ISAC — such as those in [33] — have demonstrated the effectiveness of alternating direction method of multipliers (ADMM)-based frameworks in jointly optimizing communication and radar metrics under practical constraints like peak-to-average power ratio (PAPR) and imperfect CSI. Extending such optimization methods into the DD domain for OTFS systems can be a promising research direction.

Recent studies on communication performance have introduced various techniques for channel estimation in OTFS systems [13], [27], [34]-[40][1]. The method proposed in [34] employs an embedded impulse pilot combined with high-power data, using a threshold-based approach. This pilot structure is widely recognized in OTFS literature for its effectiveness in both channel estimation and synchronization [35]-[37]. In [38], a spline interpolation step was incorporated into the threshold-based technique to improve its accuracy. The authors in [39]-[40] proposed an embedded pilot scheme that utilizes a deep learning-based approach for channel estimation. In [28], the threshold-based method has been combined with compressed sensing (CS) techniques. According to [13], the impulse-based channel estimation approach is well-suited for MU downlink and uplink scenarios. A common characteristic of these pilot structures is their PAPR, which limits the average power of the transmitted signal.

The methods of OTFS-orthogonal multiple access (OTFS-OMA) are elaborated in references [44]-[47][2]. In [44], a method using guard bands (GBs) separates resources for each user terminal (UT) in the DD domain, albeit by sacrificing reduced spectral efficiency. In contrast, Authors in [45] introduce a non-GB-based technique that allocates specific resources

[1] Additionally, there are alternative channel estimate techniques include allocate an full data frame for channel estimation [41], which could pose challenges when the channel undergoes modifications and parameters need to be updated, and superimposed pilot approaches [42], [43], where overlay pilot symbols onto data symbols inside a data frame. Nonetheless, these strategies are impractical to proposed structure; hence, we do not consider them.

[2] The NOMA method, especially in OTFS concept [48]-[50], facilitates the support of a greater number of UTs; however, it presents challenges in interference management and leads to considerable MUI. So, this paper examines the OMA method.

to UTs within the time-frequency (TF) domain, called interleaved time-frequency MA (ITFMA). Another non-GB-based technique, interleaved delay-Doppler MA (IDDMA), is proposed in [46], which ensures non-overlapping resources for the UTs in the DD domain. As both [45] and [46] demonstrate multi-user interference (MUI)-free operation using ideal pulses, the authors in [47] extend the investigation to encompass rectangular pulses. They indicate that the IDDMA can constrain focusing resource distribution in the TF domain on particular regions designated for the UTs. The IDDMA surpasses ITFMA in mitigating MUI, as data samples from each UT experience distinct and frequency-domain (FD) and TD MUI effects. The resource allocation pattern in the DD domain results in varying levels of MUI affecting the samples assigned to each UT in the TF domain due to channel disturbances. So, samples in the boundary column of TFRSs assigned to each UT exhibit more MUI than those positioned in columns further from the border. Conversely, within the ITFA, all samples in the TF domain are subjected to the same TD and FD MUI effects levels as the other UT samples. The IDDMA demonstrates superior performance compared to ITFMA regarding MUI, attributable to the distinct impacts of TD and FD on data samples. Nonetheless, ICI, ISI, and MUI continue to affect the performance of IDDMA when utilizing practical rectangular pulses.

Given the advantages and limitations of interleaving in the DD domain, as previously discussed, this paper uses a new non-GB-OMA method that employs an interleaved resource allocation strategy for ISAC-assisted downlink V2I scenarios inspired by [51]. This method effectively reduces the impact of ISI and MUI. Furthermore, based on our experience and in comparison to [47], the Zak transform is directly applicable to the proposed approach, simplifying the overall complexity of both the transmitter and receiver. Additionally, by employing a zero-padding (ZP) technique, we enhanced ISI and MUI management and utilized the padding region for pilot insertion, thereby improving the accuracy of channel estimation. In our scenario, the number of UTs is first determined during the sensing phase using a 2D correlation-based approach with a predefined adaptive threshold. In the second stage, this information is utilized to allocate resources among UTs in the DD domain and to accomplish channel estimation and data detection for each UT. This study formulates channel estimation as a sparse recovery problem. It employs the Subspace Pursuit (SP) algorithm [52] to estimate the channel parameters of the UTs, utilizing a proposed phase matrix and prior knowledge of the number of UTs. Additionally, considering the high PAPR issue of the channel estimation methods cited in [13], [27], [34]-[40], different pilot patterns, including the Zadoff-chu (Zch) sequence and the quadrature amplitude modulation (QAM) sequence, are suggested. These

methods, in addition to PAPR, offer significant benefits, including reduced ISI and MUI. Eventually, a feedback-based method adapts block linear-minimum mean square error (BL-MMSE) detectors to our method by exploiting the estimated channel parameters to recover data samples for each UT. Key contributions of the paper include the following:

- During the sensing phase, the number of UTs is accurately detected using a 2D correlation-based sensing method that incorporates a proposed adaptive threshold dependent on noise variance. Based on this detection, a non-GB-OMA framework is designed for ISAC-assisted downlink V2I communication. This framework employs a ZP strategy in combination with a unique interleaved DD resource allocation. By leveraging the Zak transform, the method not only effectively reduces MUI without requiring guard bands, but also lowers system complexity.
- By exploiting the sparse characteristics of the channel in the DD domain, we frame the channel estimation challenge as a task of sparse signal recovery. We then apply the SP technique to estimate the channel parameters using a proposed preset phase matrix. To address the PAPR issue, we also employ specifically designed pilot sequences. These sequences include a low-power Zch pilot sequence and a QAM pilot sequence, both of which demonstrate a lower PAPR compared to the traditional embedded single-pilot approach.

The content of this paper unfolds as follows. Section 2 overviews OTFS modulation, demodulation, input-out relation and the system model. Section 3 elaborates the radar sensing leveraging OTFS. Section 4 explains the non_GB_OMA method and MUI effect. Section 5 details the downlink V2I configuration. Section 6 evaluates the method via simulation, and Section 7 concludes.

Notations: Let $\boldsymbol{x}$ be a vector and $\boldsymbol{X}$ be a matrix. The r-th element of $\boldsymbol{x}$ is denoted by $x[r]$, while the element in the r-th row and c-th column of $\boldsymbol{X}$ is denoted by $X[r,c]$. Also, $vec(\boldsymbol{X})$ represents the column-wise vectorization of matrix $\boldsymbol{X}$, and $vec_{NM}^{-1}(\boldsymbol{x})$ reshapes $\boldsymbol{x}$ into a $M \times N$ matrix. Additionally, the matrix $\boldsymbol{F}_m$ represents the normalized M-point discrete Fourier transform (DFT) with $F_M[r,c] = e^{-j2\pi\left(\frac{rc}{M}\right)}$, where $r,c = 0,1,\ldots,M-1$. The matrix $\boldsymbol{F}_M^H$ corresponds to the inverse discrete Fourier transform (IDFT). Also, $\boldsymbol{I}_M$ represents the $M \times N$ identity matrix, $\square$ exhibits the matrix element-wise multiplication, $z = e^{\left(\frac{j2\pi}{MN}\right)}$, and $(r)_U$ matching to $r(\mathrm{mod}\, ulo\ U)$.

2. System Model

This paper investigates a downlink scenario within an ISAC-assisted OTFS-based V2I system, Derived from [53]. The RSU, equipped with one antenna for transmission and another for

reception, functions as a mono-static radar. Meanwhile, U single-antenna UTs serve as exclusive reflectors, as illustrated in Fig. 1. The RSU's transmit and receive antennas are effectively isolated to eliminate interference. In first stage when the number of UTs are unknown, the RSU transmits an OTFS signal to the UTs. The number of UTs is dynamically determined from the received radar echoes. This information is subsequently utilized to generate the downlink signal at the RSU and to facilitate channel estimation as well as data detection at each UT. Furthermore, the transmitted downlink signal is considered to be reflected by the UTs, producing an echo signal that can be received by the RSU. Consequently, the number of UTs can be recalculated and incorporated into the subsequent signal transmission process. The proposed framework ensures efficient resource utilization and reliable operation in scenarios involving high-mobility, capitalizing on the distinctive characteristics of OTFS in the DD domain.

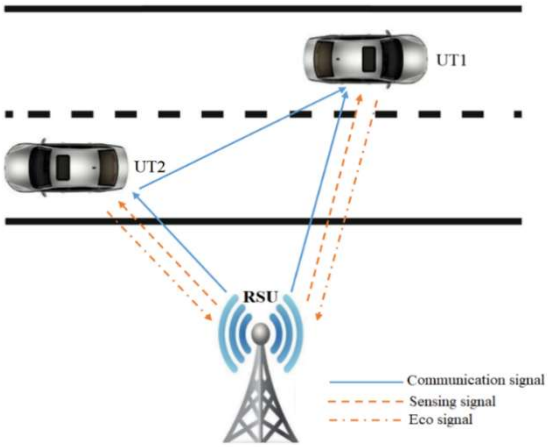

Fig. 1. ISAC-assisted OTFS in a downlink scenario.

2.1 OTFS Fundamentals

The modulation and demodulation operations in a standard Orthogonal Time Frequency Space (OTFS) system are detailed in [14]. At the transmitter, information symbols are mapped onto a two-dimensional grid in the DD domain for each OTFS frame, resulting in a symbol matrix denoted by $\left\{X_{DD}[m,n],\ m=0,\cdots,M-1,\ n=0,\cdots,N-1\right\}$, where m and n represent the discrete delay and Doppler indices, respectively. To transform $X_{DD}[m,n]$ from the DD to the TF domains, the inverse symplectic finite Fourier transform (ISFFT) [13]-[15] is deployed, as:

$$X_{TF}[l,k]=\sum_{n=0}^{N-1}\sum_{m=0}^{M-1}X_{DD}[m,n]e^{j2\pi\left(\frac{ml}{M}-\frac{nk}{N}\right)}. \quad (1)$$

Following this, the Heisenberg transform [14] is utilized to convert $\{X_{TF}[l,k],\ l=0,\cdots,M-1,\ k=0,\cdots,N-1\}$ from the TF domain to $s(t)$ in the TD for transmission through linear-time-variant (LTV) channel. The LTV channel is modelled by U distinct paths in its DD representation, indexed as $u = 0,1,\ldots,U$. The DD characterization of the channel impulse response $h(\tau,\nu)$ can be articulated as follows [13]-[16]:

$$h(\tau,\nu)=\sum_{u=1}^{U}h_u\delta(\tau-\tau_u)\delta(\nu-\nu_u), \tag{2}$$

where h_u, τ_u and ν_u indicate the channel coefficient (assumed (i.i.d)), delay shift, and Doppler shift associated with the u-th path, and $d(.)$ represents the Dirac-delta impulse pulse, respectively. Furthermore, we assert that $0<\tau_u<T$, where $T=\frac{1}{\Delta f}$ and $|\nu_u|\le\nu_{max}$ indicates the Doppler spread of the channel, which is inferior to the subcarrier spacing, Δf. The received signal, denoted as $r(t)$, is subsequently mapped to $Y_{TF}[l,k]$ through the application of the Wigner transform [13]. Eventually, the symplectic finite Fourier transform (SFFT) is applied to transition $Y_{TF}[l,k]$ into the DD domain, as:

$$Y_{DD}[m,n]=\frac{1}{\sqrt{MN}}\sum_{k=0}^{N-1}\sum_{l=0}^{M-1}Y_{TF}[l,k]e^{-j2\pi\left(\frac{ml}{M}-\frac{nk}{N}\right)}. \tag{3}$$

In radar sensing application, τ_u and ν_u can serve to extract the range and relative velocity of the u-th target, respectively. The round-trip delay τ_u and Doppler ν_u, both real numbers, [29], [30] can be defined as:

$$\tau_u=\frac{2R_u}{C}=\frac{l_u}{M\Delta f},\quad \nu_u=\frac{2f_CV_u}{C}=\frac{k_u}{NT}, \tag{4}$$

where f_c represents the carrier frequency, l_u and k_u correspond to quantization along the delay and Doppler, V_u and R_u the velocity and range of the u-th target.

2.2 Vectorized Input-Output Relationship and ZAK Transform for the Downlink Scenario

The modulating and demodulating processes in the typical OTFS system are explained in [8]. Suppose $\boldsymbol{X}$ and $\boldsymbol{Y}$ are 2D DD grids consisting of $M\times N$ QAM symbols with unit average energy. The column vectors $\boldsymbol{x}_m$ and $\boldsymbol{y}_m$ correspond to symbols located in the in m-th row of the

matrices $\boldsymbol{X}$ and $\boldsymbol{Y}$, respectively. In addition, $B = M\Delta f$ corresponds to the bandwidth and $T_f = NT$ the length of the OTFS signal frame, where $T\Delta f = 1$ (i.e., critical sampling is applied) [13], [15]. Moreover, we presume that M and N are appropriate for regarding the delay and Doppler indexes as integers.

In the downlink MU V2I scenario, the OTFS grid, representing the collection of information symbols from all UTs in the DD domain, is denoted by $\boldsymbol{X} \in \mathbb{C}^{M\times N}$. The corresponding TF domain representation, also denoted as $\boldsymbol{X}_{TF}$, is generated via the application of the inverse symplectic finite Fourier transform (ISFFT), as detailed in [13], [18], [21], [52], and is expressed as:

$$\boldsymbol{X}_{TF} = \boldsymbol{F}_M \cdot \boldsymbol{X} \cdot \boldsymbol{F}_N^H, \tag{5}$$

where $\boldsymbol{F}_M \cdot \boldsymbol{F}_M^H = \boldsymbol{I}_M$. Applying the pulse shaping matrix $\boldsymbol{G}_{tx} \in \mathbb{C}^{M\times N}$ to the delay-time (DT) domain matrix $\boldsymbol{X}_{DT} \in \mathbb{C}^{M\times N}$, and subsequently vectorizing, results in the TD transmit vector, $\boldsymbol{s} \in \mathbb{C}^{MN\times 1}$, as:

$$\boldsymbol{s} = vec\left(\boldsymbol{G}_{tx} \cdot \boldsymbol{X}_{DT}\right), \tag{6}$$

where $\boldsymbol{G}_{tx} = diag\left[g_{tx}(0),\, g_{tx}(1),\ldots,g_{tx}\left(\frac{(M-1)T}{M}\right)\right]$. The TD vector $\boldsymbol{s}$ is subjected to digital to analogue (D/A) conversion and subsequently transmitted through the LTV channel. The transmitted signal, which includes data samples from all user terminals (UTs), is reflected by multiple UTs within the coverage area, enabling each terminal to capture the composite signal and recover its intended data. The received signal vector at the u-th UT, denoted by $\boldsymbol{r}_u$ and assumed to be free of AWGN, is then processed and reformulated to construct the delay-time (DT) domain matrix as follows:

$$\boldsymbol{Y}_{u,DT} = vec_{N,M}^{-1}(\boldsymbol{I}_M \otimes \boldsymbol{G}_{u,rx}) \cdot \boldsymbol{r}_u, \tag{7}$$

where $\boldsymbol{G}_{u,rx} = diag\left[g_{u,rx}(0),\, g_{u,rx}(1),\ldots,g_{u,rx}\left(\frac{(M-1)T}{M}\right)\right]$ signifies the pulse shaping matrix at the u-th UT. This paper examines the scenario involving practical rectangular pulse shaping waveforms, Aligned with TD windowing (i.e., $\boldsymbol{G}_{tx} = \boldsymbol{G}_{rx} = \boldsymbol{I}_M$). The TF received matrix, $\boldsymbol{Y}_{u,TF} \in \mathbb{C}^{M\times N}$, is obtained by executing an M-point DFT to the columns of $\boldsymbol{Y}_{u,DT}$, as:

$$\boldsymbol{Y}_{u,TF} = \boldsymbol{F}_M \cdot \boldsymbol{Y}_{u,DT}. \quad (8)$$

The DD symbols will undergo reconstruction employing the SFFT operation as:

$$\boldsymbol{Y}_u = \boldsymbol{F}_M^H \cdot \boldsymbol{Y}_{u,TF} \cdot \boldsymbol{F}_N = \boldsymbol{Y}_{u,DT} \cdot \boldsymbol{F}_N. \quad (9)$$

The primary focus of utilizing practical rectangular pulses is to express $\mathbf{s}$ and $\boldsymbol{r}_u$ in terms of the DT samples $\boldsymbol{x}_{DT,m}$ and $\boldsymbol{y}_{u,DT,m}$ as:

$$\boldsymbol{s}[m+nM] = x_{DT,m}[n], \quad \boldsymbol{r}_u[m+nM] = y_{u,DT,m}[n]. \quad (10)$$

For this particular case, the TD samples involved in transmission and reception can be linked to the DT domain symbols as $\boldsymbol{s} = vec(\boldsymbol{X} \cdot \boldsymbol{F}_M^H)$ and $\boldsymbol{r}_u = vec(\boldsymbol{Y}_u \cdot \boldsymbol{F}_M^H)$, which can subsequently be translated into the inverse Zak transform [13], [15]. As indicated in [13], the complexity of an OTFS transmitter using Zak operations for $M > N$ is approximately $O\left(MNlog_2(N)\right)$. This approach reduces the complexity of the transmitter and receiver to performing an N-point IDFT and an N-point DFT, respectively, rendering them more straightforward in contrast to typical OTFS structure. Eventually, the input-output relation in the DD domain is formulated in vectorized form as:

$$\boldsymbol{y}_u = \boldsymbol{H}_u \cdot \boldsymbol{x}, \quad (11)$$

where $\boldsymbol{x}, \boldsymbol{y}_u \in \mathrm{C}^{MN\times 1}$. Also $\boldsymbol{H}_u \in \mathrm{C}^{MN\times MN}$ is the DD channel matrix when $\boldsymbol{x}_m, \boldsymbol{y}_{u,m} \in \mathrm{C}^{N\times 1}$ sorted and stacked as $\boldsymbol{y}_u = \left[y_{u,0}^T, y_{u,1}^T, \ldots, y_{u,M-1}^T\right]^T$ and $\boldsymbol{x} = \left[x_0^T, x_1^T, \ldots, x_{M-1}^T\right]^T$. Furthermore the TD input-output relation can be indicated as:

$$\boldsymbol{r}_u = \boldsymbol{G}_u \cdot \boldsymbol{s}, \quad (12)$$

where $\boldsymbol{s}, \boldsymbol{r}_u \in \mathrm{C}^{MN\times 1}$, and $\boldsymbol{G}_u \in \mathrm{C}^{MN\times MN}$ denote the TD channel matrix when $\boldsymbol{s}_n, \boldsymbol{r}_{u,n} \in \mathrm{C}^{M\times 1}$ sorted and stacked as $\boldsymbol{s} = \left[s_0^T, s_1^T, \ldots, s_{N-1}^T\right]^T$ and $\boldsymbol{r}_u = \left[r_{u,0}^T, r_{u,1}^T, \ldots, y_{u,N-1}^T\right]^T$. As shown in (12), $\boldsymbol{r}_u$ represents a vector that can be divided into N-block, with each block consisting of M TD samples. Consequently, the block-wise TD input-output relationship for an OTFS system is formulated as:

$$\boldsymbol{r}_{u,n} = \boldsymbol{G}_{u(n,0)} . \boldsymbol{s}_n, \quad (13)$$

where $\boldsymbol{r}_{u,n}$ denotes the n-th received block of data for $n = 0,1,\ldots,N-1$ and $\boldsymbol{G}_{u(n,0)} \in \mathrm{C}^{M\times M}$, with $(n,0)$ pertains to the n-th received block and $(n-n)$-th transmitted block, which constitute the diagonal elements of $\boldsymbol{G}_u$ [13]. The subsequent section provides an introduction to radar sensing leveraging OTFS.

3. Radar Sensing Leveraging OTFS

OTFS improves high-mobility wireless communications by modulating data in the DD domain, offering prominent potential for radar sensing applications.

3.1 2D Correlation-Based Technique

In this subsection, we introduce the 2D correlation-based parameter estimation algorithm, a method that leverages radar sensing principles to enhance target localization in high-mobility environments. In radar sensing, the RDM serves as a critical tool for detecting targets, analogous to the process of demodulating OTFS signals using rectangular pulse shaping [28]-[31]. The analogy arises because both techniques rely on resolving overlapping information in the DD domain.

Initially, RSU transmits a full frame of QAM symbols, which are modulated in the DD domain. However, despite the received OTFS symbol matrix being represented in the DD domain, interference significantly complicates the direct localization of targets from $\boldsymbol{Y}_{DD}$. This challenge stems from the fact that signals in the DD domain tend to overlap substantially after passing through the LTV channel. Such overlapping results in a mixture of channel information and interfering symbols, making it difficult to isolate individual targets or extract precise parameters. Inspired by pulse compression techniques widely employed in radar sensing, we propose a 2D correlation-based detector to address the aforementioned challenges. Pulse compression is a well-established strategy in radar systems, utilized to enhance resolution and suppress interference by leveraging the distinctive characteristics of transmitted waveforms. In a similar vein, the proposed 2D correlation-based detector performs pulse compression across the DD coordinates, thereby significantly improving the accuracy of user terminal (UT) detection. By correlating the received signal with a reference waveform in both the delay and Doppler domains, the method enables effective separation of overlapping signals and enhances the precision of parameter estimation.

Let the matrix obtained after performing 2D correlation be denoted as $\boldsymbol{V}$. This matrix represents the accumulated correlation coefficients across varying Doppler and delay indices.

Specifically, considering $Y_{DD}[m,n]$ in (3), the accumulated correlation coefficient can be declared as follows:

$$V[L,K]=\sum_{n=0}^{N-1}\sum_{m=0}^{M-1}Y_{DD}^{*}[m,n]\cdot X_{DD}[[m-L]_{M},[n-K]_{N}]. \qquad (14)$$

In Fig.2 we indicate a toy example of OTFS radar sensing with $U=4$ UTs. Fig 2(a) clarifies the real channel matrix in the DD domain. Also, Fig 2(b) shows the dense received symbol matrix in the DD domain, making UT detection difficult due to overlapping responses. After 2D correlation Fig 2(c), the UTs are more clearly localized, resembling DD domain pulse compression in radar sensing for better resolution.

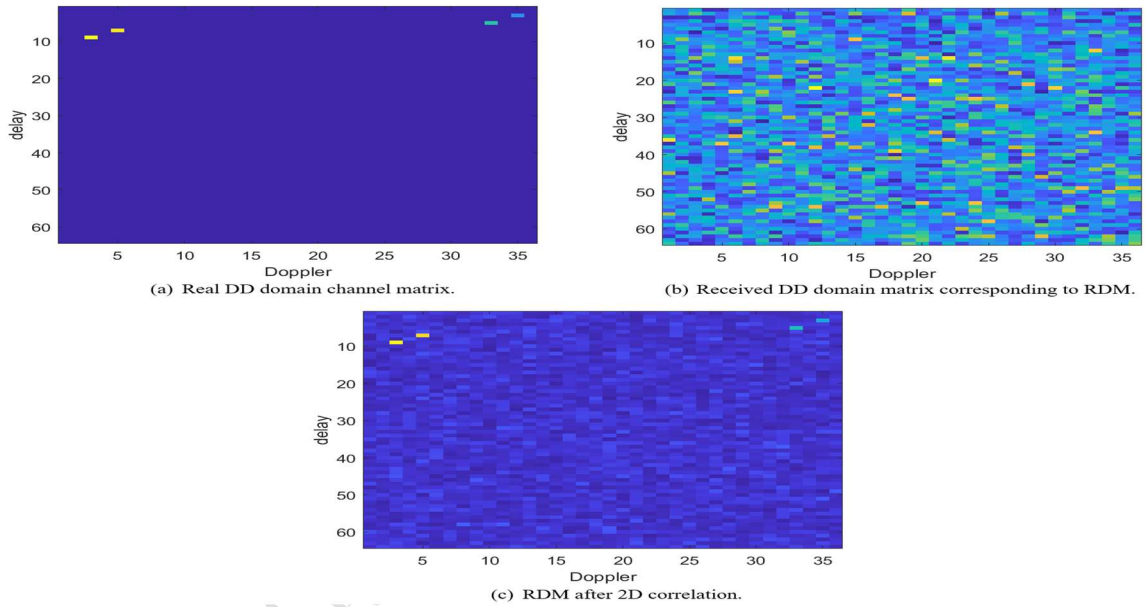

Fig. 2. (a) Real DD domain channel response, (b) the DD matrices corresponding to the RDM before applying the 2D correlation, and (c) the DD matrices after applying the 2D correlation both in the presence of AWGN with $SNR=5dB$, for $U=4$.

3.2 UT Detection via RDM

Upon acquiring the 2D correlation matrix, which captures the spatial and temporal relationships between received signals in a MU environment, the exact number of UTs remains initially indeterminate due to overlapping signal components, channel noise, and potential ambiguities in parameter estimation. To address this challenge, we have devised a robust algorithm that sequentially detects the active UTs, denoted as U by leveraging their unique signal characteristics. The algorithm focuses on UTs that differ in at least one critical parameter—

specifically, their propagation delay in this scenario—as this parameter is pivotal for distinguishing users in time-dispersive channels.

Our user detection process, outlined in Algorithm 1. The core of the detection process involves analyzing the RDM, where each row corresponds to a discrete delay index. For each row, the algorithm identifies the absolute value of the elements, which is then compared against a threshold Γ_R, serving as an indicator of a potential UT's presence at the specified delay. Motivated by [54], we select the threshold as

$$\Gamma_R = 3\sqrt{\sigma_v^2}, \tag{15}$$

where σ_v^2 refers the noise variance associated with the radar receiver. The detection process persists until no additional UTs are identified, at this point the algorithm conclusively terminates.

Algorithm 1. UT detection

1: **Input**: $M, N,$ $\boldsymbol{X}_{DD}$ (Transmit radar data frame), $\boldsymbol{Y}_{DD}$ (Received radar data frame).
2: **Output**: U.
3: Set $U = 0$;
4: **2D-correction matrix:**
5: Calculate $\boldsymbol{V}$ employing the Eq. (14);
6: **UT detection:**
5: **for** $L = 0$ to M - 1
6: **for** $K = 0$ to N - 1
7: Set the threshold Γ_R utilizing the Eq. (15);
8: **if** $|V[L,K]| \geq \Gamma_R$;
9: $U \leftarrow U + 1$;
10: **end if**
11: **end for**
12: **end for**

---

4. The non-GB-OMA Method and the Effect of MUI

In this method, each UT is allocated specific sections of delay-Doppler resource sections (DDRSs), a bin in the DD domain, which are spaced apart by a defined distance of U in the Doppler domain. The DD domain is partitioned into M and N equal segments, with the N segments being distributed across the U UTs, under the condition that M and N are even. The information symbols assigned to the u-th UT are indicated as $X_u[m,n]$, where $m = 0,1,\ldots,M-1$ and $n = 0,1,\ldots,\frac{N}{U}-1$, and they are assigned to the DDRS in the set:

$$Z_u = \left\{ (m,n) \middle| m = m',\ n = (u)_U + Up,\ for\ \ p = 0,1,\ldots,w-1,\ w = \frac{N}{U},\ m' = 0,\ldots,M-1 \right\}. \qquad (16)$$

Fig. 3(a) illustrates Z_u for $u = 0,1,\ldots,U-1$, where $U = 4$ UTs, and $M = N = 20$. Evidently, the symbols follow an interleaved arrangement within the DD domain. As illustrated in Fig. 3(b) the uniform arrangement of symbols within the DD domain confines the samples in the DT domain, once the Zak transform is applied, associated with each UT to a $(\frac{NT}{U})$ sec. × T sec. section of the DT resource sections (DTRSs). A rectangular area in the DT domain data grid, as demonstrated in Fig. 3(b), is allocated as a dedicated resource for each UT. By assigning the DDRSs from set Z_u to the u-th UT, we can derive the DT samples $X_{u,DT}[m,k]$ as:

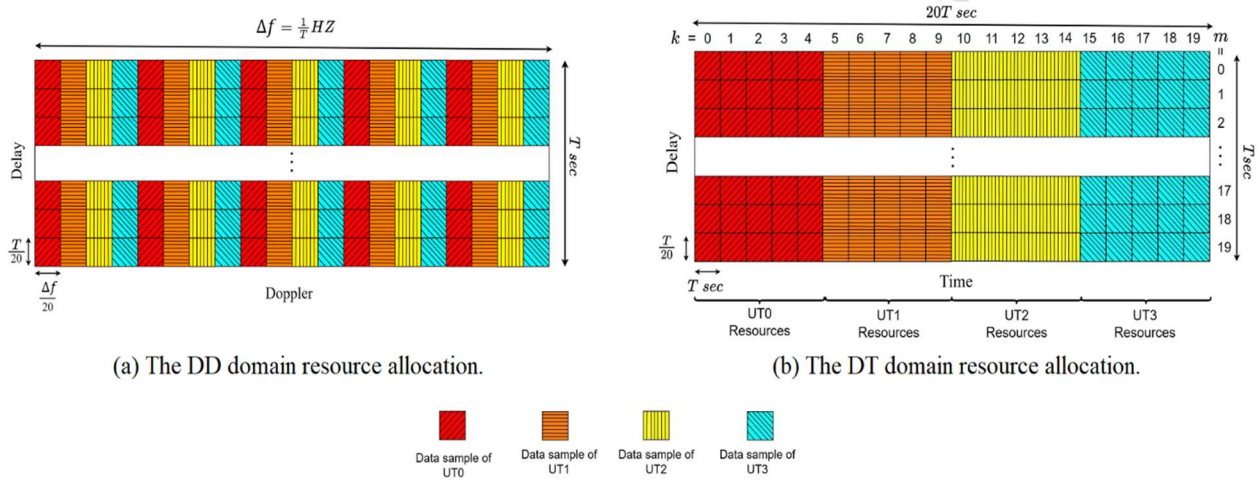

(a) The DD domain resource allocation.

(b) The DT domain resource allocation.

Fig. 3. The allocated resources for a $U = 4$ UTs scenario, (a) in the DD domain and (b) in the DT domain.

$$X_{u,DT}[m,k] = \frac{1}{\sqrt{N}} \sum_{n \in Z_u} X_u[m,n] e^{j2\pi\left(\frac{nk}{N}\right)}. \qquad (17)$$

where $k = 0,1,\ldots,N-1$ indicate the TD samples. At the receiver side, for the u-th UT, the corresponding the DD domain symbols can be reconstructed as:

$$Y_u[m,n] \triangleq \sum_{k=0}^{\frac{N}{U}-1} Y_{u,DT}[m,k] e^{-j2\pi\left(\frac{nk}{N/U}\right)}. \qquad (18)$$

Focusing on (17) and (18) reveals that the transmitter and receiver associated with the u-th UT are streamlined to and $\frac{N}{U}$-point IDFT and $\frac{N}{U}$-point DFT, respectively.

With ideal pulses, the DTRSs of different UTs remain interference-free. Nonetheless, ideal pulses are impractical, leading to the utilization of rectangular pulses. Channel path delays

cause MUI in the TD, while Doppler shifts contribute to MUI in the FD. The challenges presented by MUI in the TD and FD, intensified by LTV channels and rectangular waveforms, represent critical and pressing matters within the domain of wireless communication systems.

The IDDMA method demonstrated superior performance compared to ITFMA concerning MUI when utilizing the practical rectangular pulses [47]. Interleaved approach in the DD domain demonstrates a clear advantage over the TF domain, as ITFMA results in equal FD and TD MUI from time-frequency resource sections (TFRSs) of other UTs, irrespective of the resources allocated to each UT. The resource allocation pattern of the IDDMA in the DD domain, influenced by channel disturbances, results in varying levels of MUI for each UT within the TF domain. In IDDMA, samples located at the boundary column of resources allotted to a UT experience heightened amounts of MUI compared to those positioned further from the location. Despite its benefits, the IDDMA technique still encounters hurdles from FD and TD MUI. Our solution offers a unique approach to resource allocation by utilizing the advantages of interleaving in the DD domain.

The proposed method, as compared to the GB schemes, offers a promising alternative. The absence of a GB between different UT symbols in the DD domain, potentially improving the SE performance of the system. Furthermore, this approach demonstrates enhanced mitigation of MUI compared to non-GB-OMA methods. Through interleaving within the DD domain and the application of the Zak transform, our approach reduce system complexity. To evaluate the validity of this claim, Table 1 presents the floating-point operations (FLOPs) results of the proposed method compared to its counterpart, based on the complexity at the transmitter side for each UT.

Moreover, this approach ensures each UT encounters only TD MUI, a beneficial enhancement, as shown in Fig. 3(b). Case in point, rectangular pulses cause the DT domain samples of UT1 in the first column of DTRSs to be influenced by MUI from a single source, specifically the DT domain samples of UT0 transmitted in the preceding column (e.g., $k = 4$). This pattern also ensures that each UT experiences only the TD MUI, which is a beneficial improvement.

Table 1. The complexity of the DD non-GB-methods based on time spent at the transmitter side for each UT.

Parameters	values
Estimated FLOPs for the proposed method	0.033335 sec

Estimated FLOPs for the IDDMA method	0.060596 sec

5. Proposed Downlink Structure

The block diagram presented in Fig. 4 provides a comprehensive illustration of the proposed downlink communication V2I OTFS system. The process begins with UT detection via a 2D correlation-based sensing phase. Once the number of UTs is determined, the communication phase commences, during which the RSU maps information bits to symbols for each UT, applies proposed interleaved approach for robustness, and allocates pilot sequences for channel estimation. Using the Zak transform, symbols are mapped to the DT domain, converted to a serial format through P/S conversion, and transmitted over the LTV channel. On the receiver sides, all UTs unequivocally receive the transmitted signal and systematically carry out their individual processes. The received signal at the u-th UT which is superimposed version of the transmitted signal, is sampled and mapped to the DT domain samples after the addition of AWGN. The pilot area is then separated from data for channel estimation. The estimated parameters can be utilized for data detection in the TD. Furthermore, an additional step is used to remove pilot effects from the data in the contaminated region before the data are detected by the BL-MMSE detector, ensuring accurate and efficient correlation. Moreover, the transmitted downlink signal is analyzed to account for reflections from the UTs, resulting in echo signals that can be captured by the RSU. This allows for recalculating the number of UTs and integrating this data into the subsequent signal transmission. Our downlink structure uses ZP-OTFS, setting specific resources in the delay domain of the data grid, which includes information samples for all UTs, to zero. The ZP region along with proposed interleaved method mitigates the MUI effect. ZP-OTFS simplifies data detection and the ZP region can be utilized for pilot insertion to achieve precise channel estimation. This section presents three practical pilot patterns, followed by a discussion of the channel estimation and data detection processes.

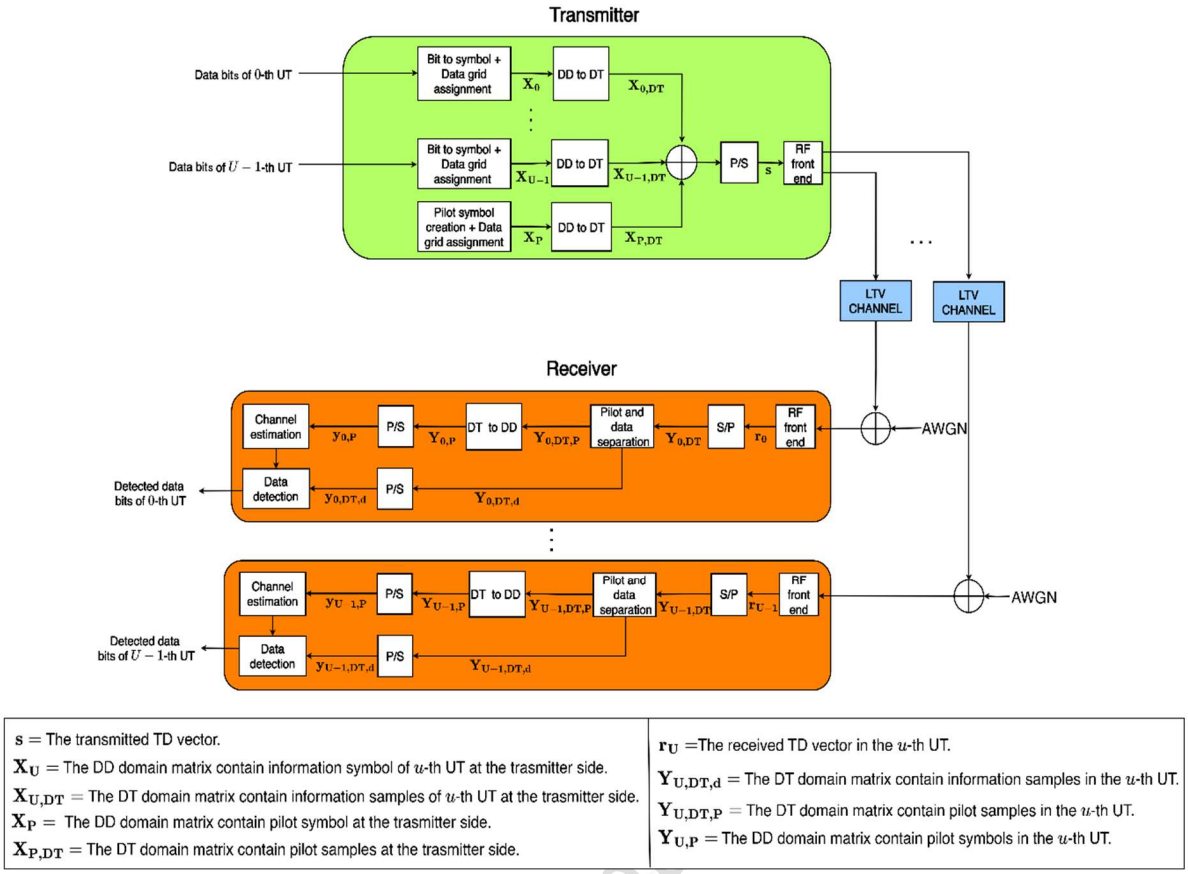

Fig. 4. Block diagram of the proposed downlink communication V2I system.

5.1 Channel Estimation and Pilot Design in the DD Domain

The effectiveness of OTFS is deeply dependent on the precision of the CSI at the receiver side. Effective estimation of the channel is essential and a requirement for evaluating the efficiency of an OTFS system.

Fig. 5 presents the frame structure of the downlink V2I scenario, wherein the final $2l_{\max}+1$ rows (the delay domain) are designated as zero to make the ZP-OTFS structure. The ZP-OTFS utilizes the padding region for the placement of pilots, facilitating channel estimation. The remaining resources are allocated to accommodate data symbols for different UTs in accordance with the proposed interleaved method. Three experimental pilot structures are utilized: the embedded single pilot method (Fig. 5(a)), the Zch sequence pilot (Fig. 5(b)), and the QAM sequence pilot (Fig. 5(c)).

The embedded pilot method, a threshold-based approach utilizing an embedded impulse, is the predominant technique for channel estimation and synchronization in OTFS literature. This method involves embedding a single high-power pilot symbol, accompanied by adequate

guard, alongside the data symbols within the data frame that contains information symbols from all UTs in the DD domain.

Let x_P represent the pilot symbol, while $X_d[m,n]$ denotes the data symbols at the coordinates $[m,n]$ within the DD data grid. Additionally, l_z is defined to represent the length of the zero region within the delay coordinate. We define $l_{\max}$ to denote the maximum delay spread, and $k_{\max}$ to represent the maximum Doppler spread among all UTs. The length of zero region is chosen based on the value of the $l_{\max}$. Fig. 5(a) demonstrates the embedded-single pilot method within a $U = 4$ UTs.

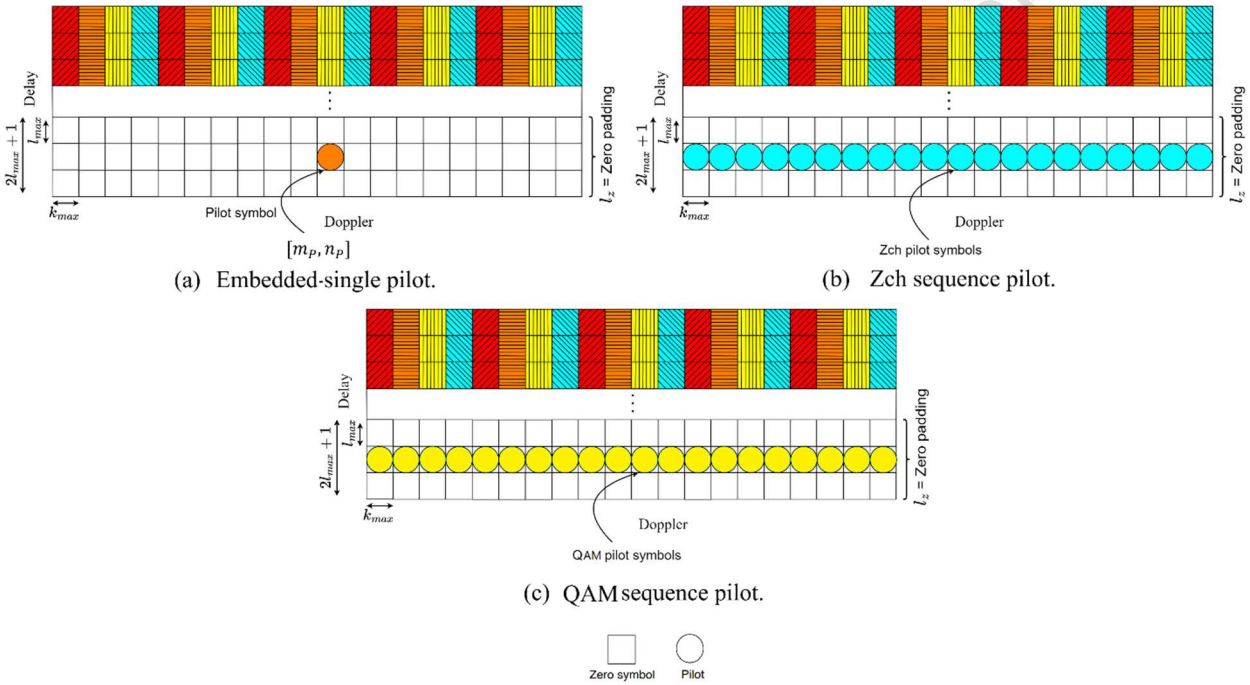

Fig. 5. Pilot insertion for the Downlink V2I, U= 4 UT, system, (a) embedded single pilot method, (b) Zch sequence pilot and (c) QAM sequence pilot.

Referring to Fig. 5(a), the pilot symbol is incorporated at the coordinates $[m_p, n_p]$, situated within the zero-padding region of the data grid at the transmitter side. At the receiver side, for channel estimation, in each UT, after separating pilot region from data, we utilize the received symbols $Y_{u,P}[m,n]$ that meet the conditions $m_P \le m \le m_P + l_{max}$ and $n_P - k_{max} \le n \le n_P + k_{max}$. The area designated as the decision region for each UT. Additionally, utilizing prior knowledge of the pilots and their locations, channel coefficients of the corresponding channel reflectors for each UT are calculated using a threshold. Subsequently, the DD shifts of the reflectors are calculated.

The embedded pilot structures experience a high PAPR caused by the utilization of a high-power pilot symbol, contributed to a reduction in the output signal's average power. This study tackles the issue by utilizing a sequence of low-power pilots and exploiting the sparse properties exhibited by the channel in the DD domain, cast the channel estimation into a sparse recovery problem.

Let reformulate vectorized input-output relation, in the DD domain, in Eq. (11), considering noise, AWGN, for the pilot sequence symbols, for the u-th UT as:

$$\boldsymbol{y}_{u,P} = \boldsymbol{X}_{u,P}\boldsymbol{h}_u + \boldsymbol{v}_u, \tag{19}$$

where $\boldsymbol{h}_u$ represents the channel vector of the u-th UT, $\boldsymbol{v}_u$ denotes the AWGN in the vector form, and $\boldsymbol{X}_{u,P}$ corresponds to our pilot matrix. The channel vector $\boldsymbol{h}_u$ has U non-zero elements out of MN and is a sparse vector. CS-based algorithms utilize channel sparsity for precise DD-domain channel estimation. The substitution of $\boldsymbol{X}_{u,P}$ with $\boldsymbol{H}_u$ in Eq. (11), in conjunction with the existence of AWGN, is clearly evident in (19). Consequently, it is imperative that $\boldsymbol{X}_{u,P}$ conforms to an equivalent structure as $\boldsymbol{H}_u$. This nudges that $\boldsymbol{X}_{u,P}$ must adhere to the ZP-OTFS channel characteristics. Furthermore, the received pilots undergo a phase shift influenced by the $k_{\max}$, and the positioning of the pilot sequence within the transmitted DD grid. To mitigate this effect, a matrix, $\boldsymbol{D}$, is generated and multiplied with the pilot matrix corresponding to different UTs. For example, for the u-th UT we can write as:

$$\boldsymbol{X}_{u,P} = \left[\left(\boldsymbol{D} \odot \boldsymbol{X}_{u,P}\right)\right], \tag{20}$$

where $\boldsymbol{D} \in \mathbb{C}^{MN \times MN}$ and is described as:

$$\boldsymbol{D} = \begin{pmatrix} \boldsymbol{D}_0 & 0 & \cdots & 0 \\ \boldsymbol{D}_1 & \boldsymbol{D}_0 & \cdots & 0 \\ \vdots & \vdots & \ddots & 0 \\ \boldsymbol{D}_{M-1} & \boldsymbol{D}_{M-2} & \cdots & \boldsymbol{D}_0 \end{pmatrix}, \tag{21}$$

where $\boldsymbol{D}_e \in \mathbb{C}^{N \times N}$ for $e = 0,1,\ldots,M-1$ represents a matrix with components described as $z^{ek(l)}$ for $l = 0,1,\ldots,N-1,$ with k being a factor dependent on $k_{\max}$.

The sparse recovery problem expresses the downlink channel estimation issue in each UT as:

$$min\left\|\boldsymbol{h}_u\right\|_0 \quad s.t \quad \boldsymbol{y}_{u,P} = \boldsymbol{X}_{u,P}\boldsymbol{h}_u + \boldsymbol{v}_u. \tag{22}$$

In this scenario, we analyze U UTs communicating with the RSU, serving as the sole reflectors concerning Doppler effects in the area. The equivalence between the number of paths and UTs allows for the application of the conventional SP algorithm to solve (22). We

reorganize the OTFS grid in the DD domain using low-power pilots distributed in the ZP region, without guard bands, alongside symbols from different UTs, as shown in Fig. 5(b) for Zch and Fig. 5(c) for QAM. This approach substitutes a high-power pilot with a sequence of low-power pilots, effectively reducing the PAPR. To estimate the channel parameters, utilizing prior knowledge of pilots for the u-th UTs, we employ the received symbols $Y_{u,P}[m,n]$ that fulfill the conditions $(M-1)-(l_{max}+1)+1 \le m \le M-1$ and $0 \le n \le N-1$, at the receiver side.

5.2 TD Data Detection

This subsection presents the feedback-based detector known as the BL-MMSE detector. This detector is distinct from the single-tap equalizer. The single-tap equalizer, while low in complexity, demonstrates effectiveness primarily in wireless channels characterized by minimal or absent mobility. High mobility induces Doppler shift, resulting in ICI and a decline in overall system performance. We will examine the BL-MMSE detector for the proposed scenario, recognized for its effective performance in both high-mobility and static channels.

By referring the block-wise TD input-output relation in (13), the BL-MMSE detector can retrieve the $\boldsymbol{s}_n$, corresponding to the u-th UT, by replacing $\boldsymbol{r}_{u,n} = \boldsymbol{y}_{u,d,n}$ and $\boldsymbol{s}_n = \boldsymbol{x}_{d,n}$, and Considering the AWGN effect as:

$$\hat{\boldsymbol{x}}_{d,n} = (\boldsymbol{G}_{u(n,0)}^{H}.\boldsymbol{G}_{u(n,0)} + \sigma_v^2 \boldsymbol{I}_M)^{-1} \boldsymbol{G}_{u(n,0)}^{H} + \boldsymbol{y}_{u,d,n}, \qquad (23)$$

where $\boldsymbol{y}_{u,d,n}$ denotes the n-th block of the received TD samples at the u-th UT, and σ_v^2 denote the noise variance. As stated in [9], ZP-OTFS can employ the L-MMSE detector in a block-wise manner, as seen in (23) for the u-th UT. At the receiver side, following the separation of the data region from the pilot signals at each UT, data detection is carried out using the received TD samples, $\boldsymbol{y}_{u,d,n}$, and the TD domain channel matrix, $\boldsymbol{G}_{u(n,0)}$. Algorithm 2 describes this process. This technique necessitates transforming merely $\frac{N}{U}$ sub-matrices of size $M \times M$ for each UT, hence diminishing the complexity of data detection.

Algorithm 2. BL-MMSE detector for the u-th UT

1: **Input**: M, N, M_{mod} (QAM alphabet), $\sigma_v^2, \boldsymbol{X}$ (Data grid style), $\boldsymbol{y}_{u,d,n}$ (received TD data of the u-th UT), $\boldsymbol{G}_{u(n,0)}$ (TD channel matrix of the u-th UT).

2: **Output**: $\hat{\boldsymbol{b}}$ (Estimated bit sequence), $\hat{\boldsymbol{x}}_{DD}$ (Estimated the DD domain symbols), $\hat{\boldsymbol{x}}_{data}$ (Estimated QAM symbols at active positions).

3: **Initialization**: $\boldsymbol{F}_N = \frac{1}{\sqrt{N}} \cdot DFT(N)$, $\boldsymbol{x} = vec(\boldsymbol{X})$, $\boldsymbol{I} = \{i \,|\, \boldsymbol{x}(i) \neq 0\}$, $\hat{\boldsymbol{X}}_d \in 0^{M \times N}$.

4: **BL-MMSE detector:**

5: **for** $n = 0$ to N - 1 do

6: Use $\boldsymbol{y}_{u,d,n} \in \mathbb{C}^{M \times 1}$ and $\boldsymbol{G}_{u(n,0)} \in \mathbb{C}^{M \times M}$;

7: Apply BL-MMSE detector based on the Eq. (23);

8: $\hat{\boldsymbol{X}}_d(:,n) \leftarrow \hat{\boldsymbol{x}}_{d,n}$;

9: **end for**

10: **Post processing:**

11: Transform to the DD domain $\hat{\boldsymbol{X}}_{DD} = \hat{\boldsymbol{X}}_d \cdot \boldsymbol{F}_N$;

12: Reshape to extract estimated QAM symbols $\hat{\boldsymbol{x}}_{DD} = vec(\hat{\boldsymbol{X}}_{DD})$, $\hat{\boldsymbol{x}}_{data} = \hat{\boldsymbol{x}}_{DD}(\boldsymbol{I})$;

13: QAM Demodulation and estimating bit sequence $\hat{\boldsymbol{b}} = QAMDe\bmod(\hat{\boldsymbol{x}}_{data}, M_{mod})$;

6. Simulation Results

For simulation purposes, two OTFS frames were generated with parameters $N = 18$, $M = 32$ and $N = 36$, $M = 64$. Furthermore, we consider the number of UTs as two distinct numbers, specifically $U = 2$ and $U = 4$, a maximum delay spread of $l_{\max} = 3$, and a maximum Doppler spread of $k_{\max} = 2$. The subcarrier spacing is $\Delta f = 15$ KHZ. Each UT employs a straightforward channel model with $U = 2$ and $U = 4$ unique delay paths randomly selected from $(0, l_{max})$, each with a random gain. Additionally, the Doppler shifts are uniformly distributed in $(-k_{\max}, k_{\max})$. Also, we have chosen the pilot' SNR of embedded single-pilot method as $SNR_P = \frac{x_P}{\sigma_v^2} = 35$ dB, and also $\Gamma_P = 3\sqrt{\sigma_v^2}$ as the embedded-single pilot threshold, where σ_v^2 refers to the noise variance at the u-th UT. Table 2 provides an overview of the simulation parameters.

In a downlink V2I scenario where PAPR is of importance, Fig. 6 exhibits the complementary cumulative distribution function (CCDF) for PAPR of the signal at two distinct SNR_P levels: 35 dB and 55 dB. The analysis considers two distinct categories of symbols characterized by different power levels: data symbols and pilot symbols. Fig .6(a) presents the evaluation results for the scenario with $U = 2$, whereas Fig .6(b) illustrates the outcomes for the scenario involving $U = 4$.

Table 2. Simulation parameters.

Parameters	values	values
M	32	64
N	18	36
U	2	4
$l_{\max}$	3	3

$k_{\max}$	2	2
$\Gamma_R = \Gamma_P$	$3\sqrt{\sigma_v^2}$	$3\sqrt{\sigma_v^2}$
Δf	15 KHZ	15 KHZ

The findings demonstrate that incorporating pilot sequences significantly improves PAPR, especially with higher SNR_P. Moreover, it highlights that Zch and QAM sequence pilots produce comparable PAPR results, both outperforming the other two approaches.

Fig. 7 depicts the mean square error (MSE) of channel estimation for the u-th UT in the downlink V2I, considering three distinct pilot insertion methods. We selected Zch sequence pilots and QAM sequence pilots, both of which share the same PAPR value and exhibit the lowest PAPR among all the pilot methods discussed.

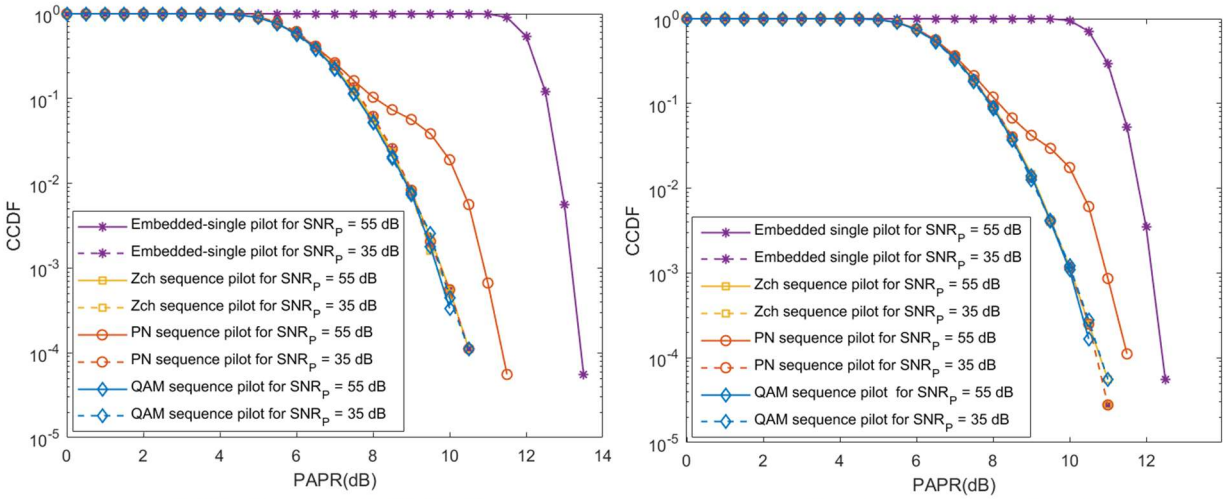

(a) For the scenario with $U = 2$. (b) For the scenario with $U = 4$.

Fig. 6. CCDF versus PAPR for two SNR_P levels 35 and 55 dB for (a) $U = 2$ and (b) $U = 4$.

Subsequently, the channel estimation results were analyzed based on the SP method for the two specified pilot structures and two distinct scenarios: Fig. 7(a), where $U = 2$, and Fig. 7(b), where $U = 4$. These results were then compared to those obtained using the embedded-single pilot channel estimation method. It is undeniable that the SP method, when employing QAM sequence pilots, delivers superior channel estimation quality compared to Zch sequence pilot.

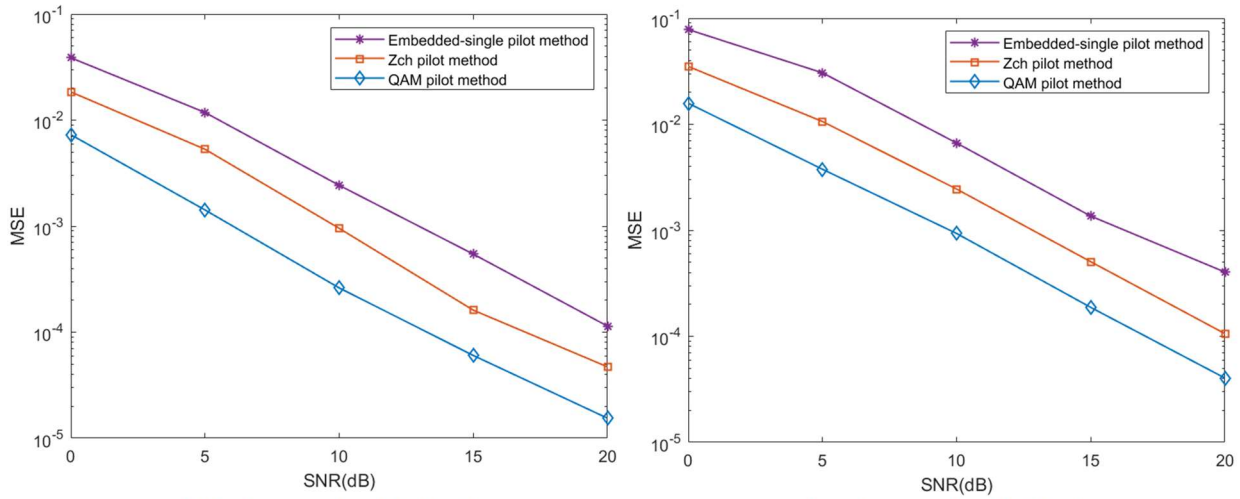

(a) For the scenario with $U = 2$. (b) For the scenario with $U = 4$.

Fig. 7. Channel estimation results for (a) $U = 2$ and (b) $U = 4$.

Fig. 8 demonstrates the bit-error rate (BER) performance of the BL-MMSE data detector for the u-th UT, employing the most effective channel estimation method: the SP technique with QAM sequence pilots. Specifically, Fig. 8(a) evaluates the BER for a system with $U = 2$, while Fig. 8(b) examines the scenario with $U = 4$, considering both 4 QAM and 16 QAM modulation techniques. The SP method, within our proposed framework, estimates channel parameters for every UT by employing a sequence of low-power pilots. Accurate CSI knowledge is critical for reliable data detection, as errors in channel parameter estimation—particularly those affecting the pilot sequence aligned with our insertion pattern—can significantly degrade detection performance.

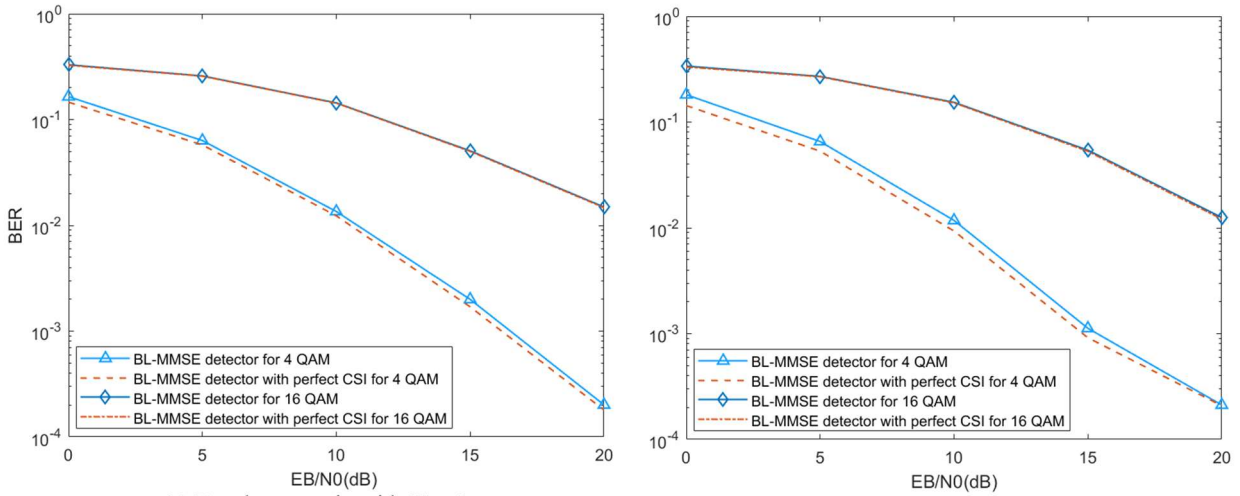

(a) For the scenario with $U = 2$. (b) For the scenario with $U = 4$.

Fig. 8. Data detection results for 4-QAM and 16-QAM for (a) $U = 2$ and (b) $U = 4$.

7. Conclusion

This paper has presented a non-GB-OMA framework for ISAC-assisted V2I networks using OTFS modulation. An interleaved resource allocation strategy, combined with a ZP mechanism, was employed to eliminate guard bands and manage MUI. The presence and the number of UTs were detected using a 2D correlation-based sensing method with an adaptive threshold. Channel estimation was formulated as a sparse signal recovery problem and addressed through the SP algorithm, supported by structured pilot patterns, a dedicated frame structure, and an external phase matrix. The PAPR was managed by incorporating the low-power Zch and QAM pilot sequences. Additionally, a two-stage feedback mechanism was integrated to adapt the BL-MMSE detector to our proposed downlink algorithm. Improvements in SNR and BER were achieved, while PAPR was effectively reduced—demonstrating the robustness and efficiency of the proposed framework in high-mobility V2I scenarios.

Data Availability. Data related to the findings in this paper can be requested from the corresponding author under reasonable conditions.

Funding. There is no funding for this work.

Conflict of Interest. The authors report the absence of any conflicts of interest.

References

[1] M. Elsharief, S. R. Sabuj, and H.-S. Jo, **"Advanced resource management strategies for next-generation 6G autonomous vehicular networks, "** 2024 *15st International Conference on Information and Communication Technology Convergence (ICTC)}*., Jeju Island, South Korea, pp. 607-608, Oct. 2024, doi: 10.1109/ICTC62082.2024.10827047.

[2] K. Ntontin, E. Lagunas, J. Querol, J. Rehman, J. Grotz, S. Chatzinotas, B. Ottersten, **"A Vision, Survey, and Roadmap Toward Space Communications in the 6G and Beyond Era,"** *Proceedings of the IEEE*, 2025, pp. 1-37. 2025, doi: 10.1109/JPROC.2024.3512934.

[3] A. Jafri and M. Jafri, "**The Development of Mobile Communications in 5G and 6G,"** *Majlesi Journal of Electrical Engineering*, vol. 15, no. 2, pp. 7-14, 2021, doi: https://doi.org/10.52547/mjtd.10.2.87

[4] P. Rajalakshmi, **"Towards 6G V2X sidelink: survey of resource allocation-mathematical formulations, challenges, and proposed solutions,"** *IEEE Open J. Veh. Technol*., vol. 5, pp. 344–383, 2024, doi: 10.1109/OJVT.2024.3368240.

[5] Y. Cui, F. Liu, X. Jing, J. Mu, **"Integrating sensing and communications for ubiquitous IoT: Applications, trends, and challenges,"** *IEEE Network*, 35(5), pp. 158–167, 2021, doi: 10.1109/MNET.010.2100152.

[6] W. Yuan, Z. Wei, S. Li, J. Yuan, D. W. K. Ng, **"Integrated sensing and communication-assisted orthogonal time frequency space transmission for vehicular networks,"** *IEEE J. Sel. Topics Signal Process.*, 15(6), pp. 1515–1528, 2021, doi: 10.1109/JSTSP.2021.3117404.

[7] C.X. Wang, X. You, X. Gao, X. Zhu, Z. Li, C. Zhang, H. Wang, Y. Huang, and Y. Chen, **"On the road to 6G: visions, requirements, key technologies and testbeds,"** *IEEE Commun. Surveys Tuts.,* 25(2), pp. 905–974, 2nd Quart. 2023, doi: 10.1109/COMST.2023.3249835.

[8] Z. Z. Yahya, D. M. Ali, and M. Y. Abdallah, **"6G automatic modulation classification using deep learning models in the presence of channel noise, CFO, and PN,"** *Majlesi Journal of Electrical Engineering*, vol. 18, no. 4, pp. 1-9, 2024, doi: https://doi.org/10.57647/j.mjee.2024.1804.59.

[9] R.L. Haupt, **Wireless communications systems: an introduction.** John Wiley and Sons, New Jersey, 2019, doi: :10.1002/9781119419204.

[10] N. Daryasafar and O. Borazjani, **"Improvement of channel estimation in MIMO-OFDM using improved LS algorithm on multipath channels, "** *Majlesi Journal of Electrical Engineering*, vol. 10, no. 3, pp. 45-52, Sep. 2016.

[11] Z. Mohammadian, M. Shahabinejad, and S. Talebi, **"A new full-diversity space-time-frequency block code for MIMO-OFDM system, "** *Majlesi Journal of Electrical Engineering*, vol. 7, no. 3, pp. 1-7, Sep. 2013.

[12] S.M. Omar, Z. Kteish, H. Fadel, **"Towards an OFDM radar waveform for detection of far located targets with relatively low radar cross sections,"** *Digit. Signal Process.,* vol. 114, pp. 103051:1–103051:13, Jul. 2021, doi: 10.1016/j.dsp.2021.103051

[13] Y. Hong, T. Thaj, E. Viterbo**, Delay-Doppler communications: principles and applications**. Academic Press, Massachusetts, 2022, doi: https://doi.org/10.1016/C2020-0-01791-3.

[14] Z. Wei, W. Yuan, S. Li, J. Yuan, G. Bharatula, R. Hadani, L. Hanzo, **"Orthogonal time-frequency space modulation: A promising next-generation waveform,"** *IEEE wireless commun.,* 28(4)*,* pp. 136-144, 2021, doi:10.1109/MWC.001.2000408.

[15] S. Li, Y. Weijie, W. Zhiqiang, H. Ruisi, A. Bo, B. Baoming, Y. Jinhong, **"A Tutorial to Orthogonal Time Frequency Space Modulation for Future Wireless Communications,"** *2021 IEEE/CIC International Conference on Communications in China (ICCC Workshops),* Xiamen, China, pp. 439-443, 2021, doi: 10.1109/ICCCWorkshops52231.2021.9538891.

[16] Z. Wei, S. Li, W. Yuan, R. Schober, G. Caire, "**Orthogonal time frequency space modulation-part I: Fundamentals and challenges ahead,"** *IEEE Communications Lett.*, 27(1), pp. 4-8, 2022, doi: 10.1109/LCOMM.2022.3209689.

[17] F. Lampel, A. Alvarado, F.M. Willems, **"Orthogonal time frequency space modulation: A discrete Zak transform approach,"** *Entropy 24(12)*, 2022. Available online: https://www.mdpi.com/1099-4300/24/12/1704, doi: https://doi.org/10.3390/e24121704.

[18] A. Farhang, A. RezazadehReyhani, L.E. Doyle, B. Farhang-Boroujeny, **"Low complexity modem structure for OFDM-based orthogonal time frequency space modulation,"** *IEEE Wireless Communications Lett., 7(3),* pp. 344–347, 2017, doi: 10.1109/LWC.2017.2776942.

[19] S. R. Sabuj, and H.-S. Jo. , **"A Complex Wavelet-Based OTFS Scheme for LEO Satellite Communication,"** in *IEEE Access*, vol. 13, pp. 85807-85825, 2025, doi: 10.1109/ACCESS.2025.3569789.

[20] R. S. Almabrouk and I. M. M. Mohamed, **"An Approach for 5G Implementation in Railways Based on Orthogonal Time Frequency Space Modulation,"** *Majlesi Journal of Electrical Engineering*, vol. 19, no. 1, pp. 1-9, Mar. 2025, doi: 10.57647/j.mjee.2025.1901.17.

[21] P. Raviteja, Y. Hong, E. Viterbo, E. Biglieri, **"Practical pulse-shaping waveforms for reduced-cyclic-prefix OTFS,"** *IEEE Trans. Veh. Technol., 68(1),* pp. 957-961. 2018, doi: 10.1109/TVT.2018.2878891.

[22] S. Li, P. Jung, W. Yuan, Z. Wei, J. Yuan, B. Bai, G. Caire, **"Fundamentals of delay-Doppler communications: Practical implementation and extensions to otfs,"** 2024, doi : https://doi.org/10.48550/arXiv.2403.14192. Available online: https:// https://arxiv.org/abs/2403.14192.

[23] S.K. Mohammed, **"Derivation of OTFS modulation from first principles,"** *IEEE Trans. Veh. Technol,* 70(8), pp. 7619-7636, 2021, doi: 10.1109/TVT.2021.3069913.

[24] L. Gaudio, M. Kobayashi, G. Caire, G. Colavolpe, **"On the effectiveness of OTFS for joint radar parameter estimation and communication,"** *IEEE Trans. Wireless Commun.,* 19(9), pp.5951–5965, 2020, doi: 10.1109/TWC.2020.2998583.

[25] P. Raviteja, K. T. Phan, Y. Hong and E. Viterbo**, "Orthogonal time frequency space (OTFS) modulation based radar system,"** *2019 IEEE Radar Conf.,* (RadarConf), pp. 1–6, 2019, doi: 10.1109/RADAR.2019.8835764.

[26] M. F. Keskin, H. Wymeersch, A. Alvarado, **"Radar sensing with OTFS: Embracing ISI and ICI to surpass the ambiguity barrier,"** *2021 IEEE Int. Conf. Commun. Work. ICC Work.,* 2021-Proc., 2021, doi: 10.1109/ICCWorkshops50388.2021.9473534.

[27] Z. Tang, L. Yu, **"A Method of Interference Suppression in Integrated OTFS Communication and Sensing Systems,"** *IEEE Access.,* pp.144044–144054, 2024, doi: 10.1109/ACCESS.2024.3470896.

[28] F. Liu, C. Masouros, Y. C. Eldar, **Integrating sensing and communication.** Springer, 2023, doi: https://doi.org/10.1007/978-981-99-2501-8

[29] K. Zhang, Z. Li, W. Yuan, Y. Cai, F Gao, **"Radar sensing via OTFS signaling,"** *China Communications.,* 20(9), pp. 34–45, 2023, doi: 10.23919/JCC.fa.2023-0060.202309.

[30] J. Zhang, L Cai, H. Liu, **"Integrated sensing and communication via orthogonal time frequency space signaling with hybrid message passing detection and fractional parameter estimation,"** *Sensors.,* 23(24), 9874, 2023, doi: https://doi.org/10.3390/s23249874. Available online: https://www.mdpi.com/1099-4300/25/9/1358.

[31] T. Long, Y. Weijie, Z. Xiaoqi, Z. Kecheng, L. Zhongjie,L. Yonghui, **"DNN-Based Radar Target Detection With OTFS,"** *IEEE Transactions J. Vehicular Technology.,* pp. 1–6, 2024, doi: 10.1109/TVT.2024.3408059.

[32] M. Delamou, A. Bazzi, M. Chafii, and E. M. Amhoud, **"Deep learning-based estimation for multitarget radar detection,"** in *Proc. IEEE 97th Veh. Technol. Conf. (VTC2023-Spring)*, Florence, Italy, pp. 1–5, 2023, doi: 10.1109/VTC2023-Spring57618.2023.10200157.

[33] A. Bazzi, M. Chafii, **"On integrated sensing and communication waveforms with tunable PAPR, "** *IEEE Trans. Wireless Commun.* , 22(11), pp. 7345–7360, Nov. 2023, doi: 10.1109/TWC.2023.3250263.

[34] P. Raviteja, K.T. Phan, Y. Hong, **"Embedded pilot-aided channel estimation for OTFS in delay-Doppler channels,"** *IEEE Trans. Veh. Technol*, 68(5), pp. 4906-4917, May 2019, doi: 10.1109/TVT.2019.2906357.

[35] S.G. Neelam, P. Sahu, **"Channel estimation and data detection of OTFS system in the presence of receiver IQ imbalance,"** *in 2021 National Conference on Communications (NCC),* pp. 1-6, 2021, doi: 10.1109/NCC52529.2021.9530106.

[36] Y. Liu, S. Zhang, F. Gao, J. Ma, X. Wang, **"Uplink-aided high mobility downlink channel estimation over massive MIMO-OTFS system,"** *IEEE J. Select. Areas Commun.,* 40(1), pp. 5–36, Jan. 2022, doi: 10.1109/JSAC.2020.3000884.

[37] Y. Liu, Y.L. Guan, D. Gonz´alez, **"Near-optimal bem OTFS receiver with low pilot overhead for high-mobility communications,"** *IEEE Tran. Commun.,* 70(5), pp. 3392-3406, 2022, doi: 10.1109/TCOMM.2022.3162257.

[38] T. Thaj, E. Viterbo, Y. Hong, **"Orthogonal time sequence multiplexing modulation: Analysis and low-complexity receiver design,"** *IEEE Trans. Wireless Commun.,* 20(12), pp. 7842-7855, 2021, doi: 10.1109/TWC.2021.3088479.

[39] X. Zhang, H. Wen, Z. Yan, W. Yuan, J. Wu, and Z. Li, **"A novel joint channel estimation and symbol detection receiver for orthogonal time frequency space in vehicular networks,"** *Entropy,* 25(9), 2023, https://doi.org/10.3390/e25091358. Available online: https://www.mdpi.com/1099-4300/25/9/1358.

[40] Q. Li, Y. Gong, F. Meng, Z. Li, L. Miao and Z. Xu, **"Residual learning based channel estimation for OTFS system,"** 2022 IEEE/CIC International Conference on Communications in China (ICCC Workshops)., Sanshui, Foshan, China, pp. 275–280, 2022, doi: 10.1109/ICCCWorkshops55477.2022.9896637.

[41] M.K. Ramachandran, A. Chockalingam, **"MIMO-OTFS in high-Doppler fading channels: Signal detection and channel estimation,"** *2018 IEEE Global Communications Conference (GLOBECOM)*, IEEE, pp. 206-212, 2018, doi: 10.1109/GLOCOM.2018.8647394

[42] O.A. Aghda, M.J. Omidi, H. Saeedi-Sourck, **"Superimposed channel estimation in OTFS modulation using compressive sensing,"** *2023 31st International Conference on Electrical Engineering (ICEE),* Tehran, Iran, Islamic Republic of, pp. 756-761, 2023, doi: 10.1109/ICEE59167.2023.10334727.

[43] H. B. Mishra, P. Singh, A. K. Prasad and R. Budhiraja, **"OTFS channel estimation and data detection Designs with superimposed pilots,"** *IEEE Trans. Wireless Commun,* 21(4), pp. 2258-2274, 2022, doi: 10.1109/TWC.2021.3110659.

[44] S. Rakib and R. Hadani, **"Multiple access in wireless telecommunications system for high-mobility applications,"** U.S. Patent 9 722 741 B1, Aug. 2017.

[45] R.M. Augustine, A. Chockalingam, **"Interleaved time-frequency multiple access using OTFS modulation,"** *2019 IEEE 90th Vehicular Technology Conference (VTC2019-Fall),* pp. 1-5, 2019, doi: 10.1109/VTCFall.2019.8891404.

[46] V. Khammammetti, S.K. Mohammed, **"OTFS-based multiple-access in high Doppler and delay spread wireless channels,"** *IEEE Wireless Communications Lett.,* 8(2), pp. 528–531, 2018, doi: 10.1109/LWC.2018.2878740.

[47] V. Khammammetti, S.K. Mohammed, "**Spectral efficiency of OTFS based orthogonal multiple access with rectangular pulses,**" IEEE Transactions J. Vehicular Technology., vol. 71(12), pp. 12989–13006, 2022, doi: 10.1109/TVT.2022.3199478.

[48] Z. Ding, R. Schober, P. Fan, H.V. Poor, **"OTFS-NOMA: An efficient approach for exploiting heterogeneous user mobility profiles,"** *IEEE Trans. Commun.,* 67(11), pp. 7950-7965, 2019, doi: 10.1109/TCOMM.2019.2932934.

[49] K. Deka, A. Thomas, S. Sharma, **"OTFS-SCMA: a code-domain NOMA approach for orthogonal time frequency space modulation,"** *IEEE Tran. Commun.,* 69(8), pp. 5043-5058, 2021, doi: 10.1109/TCOMM.2021.3075237.

[50] B.C. Pandey, S.K. Mohammed, P. Raviteja, Y. Hong, E. Viterbo, **"Low complexity preceding and detection in multi-user massive MIMO OTFS downlink,"** *IEEE trans. Veh. Technol.,* 70(5), pp. 4389-4405, 2021, doi: https://doi.org/10.48550/arXiv.2011.12241

[51] G. Saeidi, H. Saeedi-sourk, **"A ZP-OTFS-based interleaved non-GB-OMA method for uplink communication,"** 2024, doi: https://doi.org/10.21203/rs.3.rs-3821149/v1. Available: https://www.researchsquare.com/article/rs-3821149/v1.

[52] W. Dai, O. Milenkovic, **"Subspace pursuit for compressive sensing signal reconstruction,"** *IEEE transactions J. Information Theory.,* 55(5), pp. 2230–2249, 2009, doi: 10.1109/TIT.2009.2016006.

[53] W. Yuan, Z. Wei, S. Li, J. Yuan, D.W.K. Ng, **"Integrated sensing and communication-assisted orthogonal time frequency space transmission for vehicular networks,"** *IEEE J. Sel. Topics Signal Process.*, 15(6), pp. 1515–1528, 2021, doi: 10.1109/JSTSP.2021.3117404.

[54] W. Yuan, S. Li, Z. Wei, J. Yuan, D.W.K. Ng, **"Data-aided channel estimation for OTFS systems with a superimposed pilot and data transmission scheme, "** *IEEE Wireless Communications Lett.,* 10(9), pp. 1954-1958 , 2021, doi: 10.1109/LWC.2021.3088836.